APPLIED SCIENCES AND ENGINEERING

Layer- and gate-tunable spin-orbit coupling in a high-mobility few-layer semiconductor

Dmitry Shcherbakov[1], Petr Stepanov[1], Shahriar Memaran[2], Yaxian Wang[3], Yan Xin[2], Jiawei Yang[1], Kaya Wei[2], Ryan Baumbach[2], Wenkai Zheng[2], Kenji Watanabe[4], Takashi Taniguchi[5], Marc Bockrath[1], Dmitry Smirnov[2], Theo Siegrist[2], Wolfgang Windl[3], Luis Balicas[2], Chun Ning Lau[1]*

Spin-orbit coupling (SOC) is a relativistic effect, where an electron moving in an electric field experiences an effective magnetic field in its rest frame. In crystals without inversion symmetry, it lifts the spin degeneracy and leads to many magnetic, spintronic, and topological phenomena and applications. In bulk materials, SOC strength is a constant. Here, we demonstrate SOC and intrinsic spin splitting in atomically thin InSe, which can be modified over a broad range. From quantum oscillations, we establish that the SOC parameter α is thickness dependent; it can be continuously modulated by an out-of-plane electric field, achieving intrinsic spin splitting tunable between 0 and 20 meV. Unexpectedly, α could be enhanced by an order of magnitude in some devices, suggesting that SOC can be further manipulated. Our work highlights the extraordinary tunability of SOC in 2D materials, which can be harnessed for in operando spintronic and topological devices and applications.

INTRODUCTION

In a crystal, the twofold degeneracy of spins is protected by the combined inversion symmetry in both space and time. In the well-known Zeeman effect, an external magnetic field breaks the time reversal symmetry (TRS) and splits the spin degeneracy by $g\mu_B B$, where g is the gyromagnetic ratio and μ_B is Bohr magneton. Alternatively, spin degeneracy can be lifted by spin-orbit coupling (SOC) when spatial inversion symmetry is broken, even in the absence of a TRS-breaking magnetic field. In crystals lacking structural inversion symmetry, the SOC coupling is of the Rashba form, $H_R = \alpha/\hbar(\hat{z} \times \boldsymbol{p})\cdot\boldsymbol{\sigma}$, where α is the Rashba parameter, $\boldsymbol{p}$ is the momentum, and $\boldsymbol{\sigma}$ is the Pauli spin matrices (*2*, *3*). As a result, the energy band of the crystal is spin-split; within each subband, the charges' spin is locked to their direction of momentum (Fig. 1A). A large SOC can be used to manipulate spins and generate interesting phenomena (*4*–*6*), such as the spin Hall effect, spin-orbit torque, and topological phenomena including the quantum spin Hall effect and quantum anomalous Hall effect.

The advent of two-dimensional (2D) materials provides platforms with unprecedented opportunities for SOC tuning. For instance, sizable SOC can be "endowed" to graphene by proximitization with transition metal dichalcogenides (*7*–*19*), and intrinsic SOC in 2D semiconductors has been studied by weak-antilocalization measurements (*20*–*22*). Here, we exploit the atomically thin sheets of InSe to demonstrate the extraordinary tunability of SOC in 2D materials.

InSe is a layered semiconductor with thickness-dependent bandgaps that range from 1 to 3 eV. Its direct bandgap (except in monolayers), combined with extraordinarily high mobility (*23*, *24*), makes it a very attractive electronic and optoelectronic material. The 2D unit cell of an InSe monolayer is composed of two vertically aligned In atoms, sandwiched between two planes of Se atoms. When projected onto a plane, an InSe monolayer forms a honeycomb lattice, where the metallic and chalcogen atoms occupy the two sublattices, respectively (Fig. 1B). Bulk crystals of InSe are found in several polytypes, including γ, β, ε, and δ phases (*25*). In this study, crystals are grown by the Bridgeman technique and are confirmed by a transmission electron microscope (TEM) to be predominantly γ phase with rhombohedral stacking, though stacking faults and nanotwins are rather common (see the Supplementary Materials). The γ phase belongs to the space group *R3m* and is noncentrosymmetric; this lack of inversion symmetry is a key ingredient that allows SOC-induced spin-split bands in the absence of an external magnetic field. Although SOC in InSe has been measured via weak-localization studies on relatively thick flakes (*20*, *22*), the values obtained have relatively large error bars, while the single-gated devices do not allow independent tuning of the Rashba SOC.

Our devices consist of atomically thin InSe sheets with thicknesses ranging from four to 10 layers (Table 1) and sandwiched between hexagonal BN (hBN) layers, with few-layer graphene (FLG) contacts, a silicon back gate, and a metal top gate (Fig. 1C). By varying voltages applied to the top gate V_{Tg} and back gate V_{Bg}, we can independently control the charge density $n = \frac{1}{e}(C_{Bg}V_{Bg} + C_{Tg}V_{Tg})$ and out-of-plane electric field $E_\perp = \frac{C_{Tg}V_{Tg} - C_{Bg}V_{Bg}}{2\varepsilon_0}$. Here, C_{Tg} and C_{Bg} are capacitance per unit area between the gates and InSe, e is the electron charge, and ε_0 is the permittivity of vacuum. We note that the application of $E_\perp$ is particularly crucial for modulation of Rashba SOC strength, which, depending on the direction of application, can either further break the inversion symmetry or compensate for the built-in asymmetry of the lattice.

RESULTS AND DISCUSSION

Figure 1D presents the longitudinal resistance R_{xx} of device D1, which has a thickness of ~6 layers, as a function of back gate voltage and magnetic field B. A prominent Landau fan is observed. Shubnikov de Haas (SdH) oscillations start at B as low as 2.5 T, indicating a

[1]Department of Physics, The Ohio State University, Columbus, OH 43210, USA. [2]National High Magnetic Field Laboratory, Tallahassee, FL 32310, USA. [3]Department of Materials Science and Engineering, The Ohio State University, Columbus, OH 43210, USA. [4]Research Center for Functional Materials, National Institute for Materials Science, 1-1 Namiki, Tsukuba, Ibaraki 305-0044, Japan. [5]International Center for Materials Nanoarchitectonics, National Institute for Materials Science, 1-1 Namiki, Tsukuba, Ibaraki 305-0044, Japan.
*Corresponding author. Email: lau.232@osu.edu

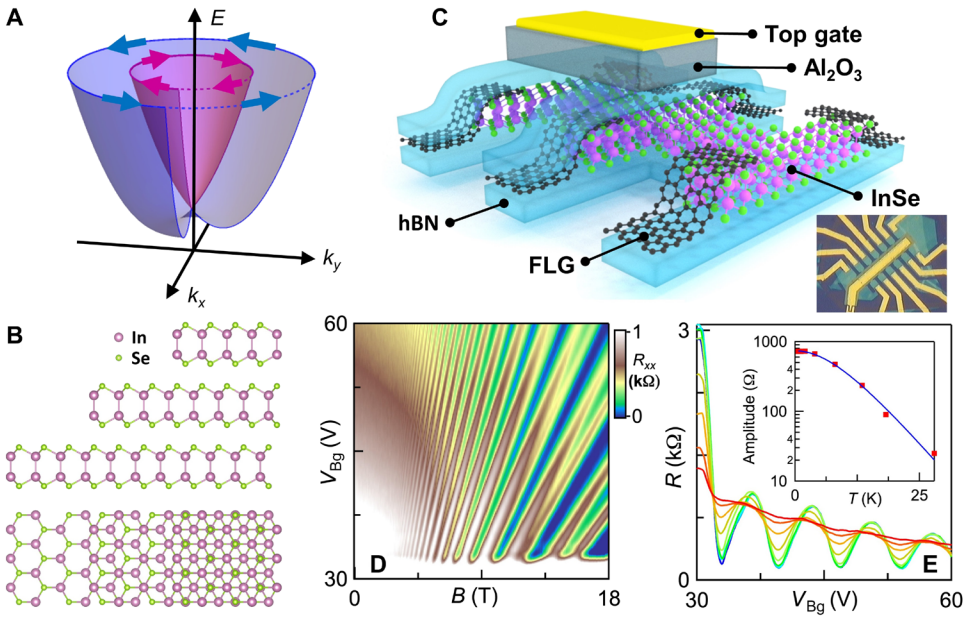

Fig. 1. Crystal structure, device schematics, and magnetotransport data. (**A**) Rashba SOC–induced spin splitting of bands. (**B**) Side and top views of the crystalline structure of γ-InSe. The middle and bottom layers are partially exposed for better visualization [images created using VESTA software (*1*)]. Inset: Optical image of a device. (**C**) Schematics of device structure. (**D**) Landau fan $R_{xx}(V_{Bg}, B)$ of device D1 from $B = 0$ to 18 T. (**E**) SdH oscillations at $B = 10$ T for temperatures ranging from 0.6 to 28 K. Inset: Amplitude of the oscillations as a function of temperature. The line is a fit to the Lifshitz-Kosevich formula.

Table 1. Device parameters.

Device	Estimated thickness	α_0 (10^{-11} eV m)	α' (10^{-2} e nm^2)
D1	Six-layer	3.5	3.0
D2	Four-layer	0.6	−1.2
D3	Seven-layer	0.2	−1.2
D3	Eight-layer	0.15	−1.15
D3	Nine-layer	0.08	−1.1
D4	Six-layer	0.3	1.1
D5	Four-layer	0.8	1.3

quantum mobility exceeding 4000 cm^2/Vs, which is the highest value reported to date. At $B > 12$ T, quantized plateaus for filling factor $\nu < 10$ are observed. To estimate the effective mass of the charge carriers, we extract the amplitude A of the SdH oscillations at $B = 10$ T at different temperatures (Fig. 1E). From the Lifshitz-Kosevich equation, $A = CT/\sinh(bT)$, where T is the temperature, $b = \frac{2\pi^2 k_B T}{\hbar \omega_c}$, $\omega_c = \frac{eB}{m^* m_0}$ is the cyclotron frequency, m^* is the reduced effective mass, m_0 is the rest mass of electrons, k_B is the Boltzmann constant, $\hbar$ is the reduced Planck constant, and C is a constant, we estimate that $m^* \sim 0.14$, in excellent agreement with prior reports (*23*, *24*). Similar measurements on 4-layer and 10-layer devices yield $m^* = 0.15$ and 0.13, respectively. Thus, we will use $m^* = 0.14$ throughout the rest of the manuscript.

The high device mobility enables manifestation of the hallmark of Rashba SOC—in 2D conductors with spin-split bands, the different concentrations of spin-up and spin-down electrons give rise to a characteristic beating pattern in the SdH oscillations. Figure 2A displays dR_{xx}/dB for device D2, which is estimated to be ~4 layers thick, as a function of n and B at a constant $E_\perp = -0.33$ V/nm, where the nodes in the oscillations appear as a white band for B ~4 to 6 T. A line cut of $dR_{xx}/dB(B)$ at $n = 7 \times 10^{12}$ cm^{-2} is shown in Fig. 2B, where the nodes are indicated by the arrows. The presence of two distinct frequencies is clearly reflected in the Fourier transform of the data (Fig. 2C), where we observe two distinct peaks in $1/B$, and the separation between the two peaks is larger at higher charge density.

Intriguingly, the parity of the oscillations changes after crossing the nodes—as shown in Fig. 2B inset, as B increases, the conductance minima at a fixed filling factor become maxima and vice versa. Since the degeneracy of the oscillations is two at these fields, such a change in parity indicates that only odd integer states are resolved for B below the nodes, and even integer states for B above the nodes.

The beating pattern, the beating frequency that scales linearly with charge density, and the alternating parities in the SdH oscillations are the hallmark signatures of large Rashba SOC in a 2D semiconductor, in which the quadratic band is spin-split by $\Delta_R = 2|\alpha k_F|$ (here, k_F is the Fermi momentum). The different Fermi surface areas of spin-up and spin-down bands give rise to different oscillation frequencies, which interfere to generate the characteristic beating pattern. The Landau level (LL) spectrum is then given by (*2*, *3*, *6*)

$$E_N^{\pm} = \hbar\omega_c \left[N \pm \frac{1}{2}\sqrt{(1 - gm^*/2)^2 + N\frac{\Delta_R^2}{E_F \hbar \omega_c}} \right], E_0 = \frac{1}{2}\hbar\omega_c \quad (1)$$

Here, N is the LL index, E_F is the Fermi energy, and g is the effective g-factor. Figure 2F plots the LL spectrum for $N = 0$ to 10. Pronounced

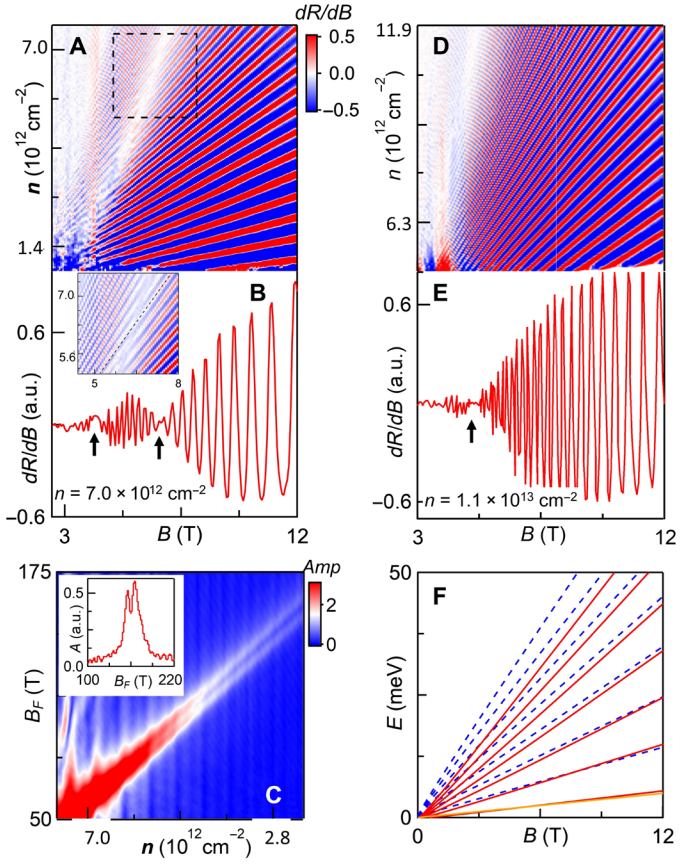

Fig. 2. Beating patterns in SdH oscillations from device D2 at $T = 0.3$ K. (**A**) $dR_{xx}/dB(n, B)$ at $E_\perp = 0.33$ V/nm. (**B**) Line trace of (A) at $n = 7.0 \times 10^{12}$ cm^{-2}. Arrows indicate nodes of oscillations. Inset: Zoom-in plot of the dashed square in (A). Dashed line indicates the transition from minima to maxima. a.u., arbitrary units. (**C**) Fast Fourier transform of the data in (A), display two distinct frequencies. Inset: line trace of fast Fourier transform amplitude versus B_F at $n = 2.8 \times 10^{12}$ cm^{-2}. (**D**) $dR_{xx}/dB(n, B)$ at $E_\perp = 0$. (**E**) Line trace of (D) at $n = 1.1 \times 10^{13}$ cm^{-2}. (**F**) LL energies calculated using Eq. 1 and $\alpha = 1.0 \times 10^{-11}$ eVm. The orange line denotes the zeroth LL, whereas the red solid and blue dashed lines represent spin-up and spin-down levels for $N > 0$.

LL crossings occur between spin-split bands. Notably, the Rashba SOC strength can be extracted from the beating patterns

$$\alpha \approx \frac{\hbar^2}{m^* m_0}\sqrt{\frac{\pi}{2}}\frac{\Delta n}{\sqrt{n}} \quad (2)$$

where $\Delta n = (e/h)B_{F,\mathrm{beat}}$ is the difference in densities between majority and minority spin carriers and $B_{F,\mathrm{beat}}$ is the beating frequency in SdH oscillations. Using Eq. 2, we estimate that $\alpha \sim 0.9 \times 10^{-11}$ eV m for the dataset shown in Fig. 2, A to C.

Since Rashba SOC is a consequence of broken inversion symmetry, we expect that an externally applied $E_\perp$ can either induce additional asymmetry or compensate for the inversion symmetry of the lattice, thus providing an experimental knob to tune the SOC strength in situ. This is borne out experimentally—a similar dataset of device D2 taken at $E_\perp = 0$ (Fig. 2D) displays a substantially different beating pattern: Comparing with that at $E_\perp = -0.33$ V/nm, the nodes shift to smaller B, indicating that the SOC strength is reduced.

To systematically examine the variation of SOC with $E_\perp$, we measure R_{xx} of device D2 as a function of n and $E_\perp$ at constant $B = 6$ T (Fig. 3A). As $E_\perp$ varies, the oscillations' maxima clearly transition into minima and vice versa; the transition points move approximately linearly on the n-$E_\perp$ plane. In the SdH oscillations regime, the magnetoresistance of the device is related to the LL spectrum by (*26*)

$$\rho_{xx} \sim B^2\sigma_{xx} \sim B^2\Sigma\left(N \pm \frac{1}{2}\right)e^{-\left(E_F - E_N^{\pm}\right)^2/\Gamma^2} \quad (3)$$

where E_F is the Fermi energy and Γ is the LL broadening. We model the effect of the electric field by taking

$$\alpha = |\alpha_0 + \alpha' E_\perp| \quad (4)$$

where α is the "intrinsic" Rashba parameter, arising from the asymmetry of the intrinsic lattice and/or the confining potentials, including the different dielectric thicknesses for the gates; α' parametrizes the effectiveness of the electric field at tuning the SOC coupling, which can be positive or negative, depending on the field's orientation relative to the built-in inversion asymmetry of the lattice. Combining Eqs. 1 and 3, and assuming $\Gamma = 1$ meV, $m^* = 0.14$, we are able to satisfactorily reproduce the data by using $\alpha = 0.6 - 1.2\,E_\perp$, where α is in unit of 10^{-11} eVm and $E_\perp$ in V/nm (Fig. 3B). Magnitude of these values agrees with those obtained from density functional theory (DFT) calculations (Fig. 4D) (*27*, *28*). Together, these results underscore the highly tunable nature of the Rashba SOC in a 2D semiconductor, which, by applying an external $E_\perp$, can be enhanced, reduced, and even completely suppressed to zero.

A unique opportunity afforded by the atomically thin 2D membranes is the exploration of SOC in a layer-by-layer fashion. To this end, we fabricate devices on a single piece of InSe flake with adjacent regions that differ by a single atomic layer in thickness (see Supplementary Materials). Figure 3 (C to E) presents data for such a device D3, which hosts regions that are estimated to be seven, eight, and nine layers, respectively. The overall features in the $dR_{xx}/dn(n, E_\perp)$ plots at $B = 6$ T are qualitatively similar, with an important difference: As the thicknesses increase, the transition points shift to lower (more negative) $E_\perp$ values. These patterns can be satisfactorily captured by our simulations, yielding the intrinsic Rashba parameter $\alpha_0 = 0.2 \times 10^{-11}$, 0.15×10^{-11}, and 0.08×10^{-11} eVm, respectively, for the regions that are seven, eight, and nine layers thick; α', the effective tunability of the SOC, is extracted to be -1.2×10, -1.15×10, and -1.1×10 e nm^2, respectively. Thus, as the layer number increases, both the intrinsic SOC strength and its scaling with external $E_\perp$ are diminished (*27*). This trend is opposite to that predicted by theory calculations (*28*). Such discrepancy is not understood at this point and should stimulate further theoretical and experimental works to explore, for example, variations of hopping parameters with number of layers, variations of intra- and interlayer SOC with energy, and effects of electron interactions and screening. The strength and tunablility of the Rashba SOC of different devices are summarized in Fig. 4C.

Last, we observe that some devices appear to be markedly enhanced. Figure 4A presents $dR_{xx}/dn(n, E_\perp)$ at $B = 10$ T for device D1. Notably, instead of a single transition point at a given n, several crossing points are visible. Such large number of transitions indicates much higher SOC—we are able to reproduce the patterns by taking $\alpha = 3.5 + 3.0\,E_\perp$ (Fig. 4B). Compared to values in the previous plots, α' increases by as much as an order of magnitude, while tunability α' is enhanced by a factor of 3. Such a large SOC strength is unexpected and unlikely to originate from variations such as thicknesses of flake or gate dielectrics. Instead, it suggests a fundamental mechanism at play. One possibility is variations in the interlayer spacing

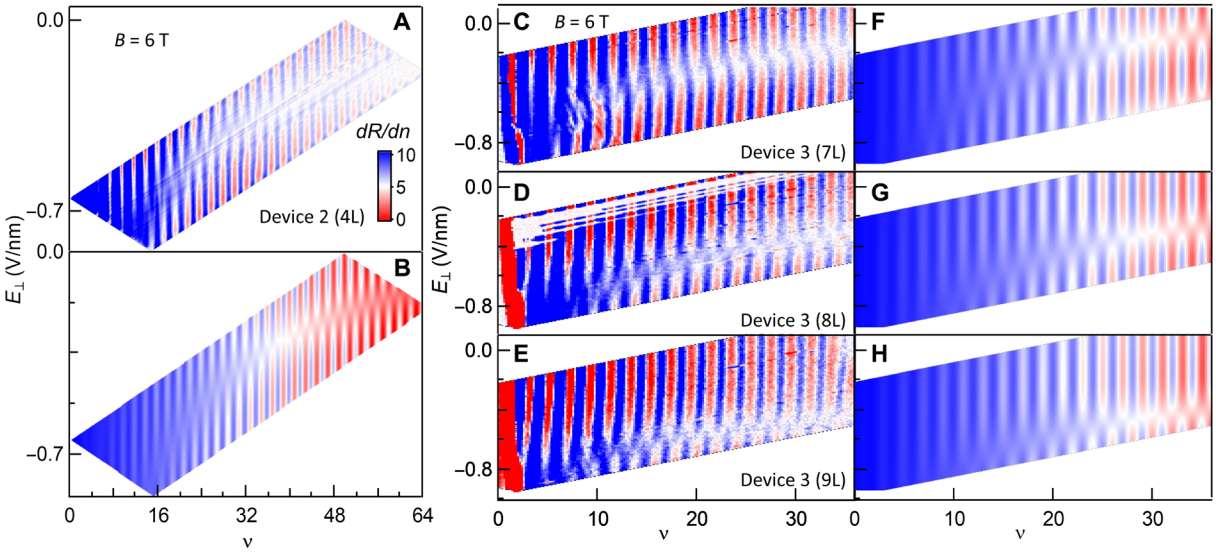

Fig. 3. Magnetotransport data $dR_{xx}/dn(n, E_\perp)$ at constant B. (**A** and **B**) Data and simulation for device D2. (**C** to **E**) Data for different regions of device D3 that are seven, eight, and nine layers thick, respectively. (**F** to **H**) Simulations for device D3.

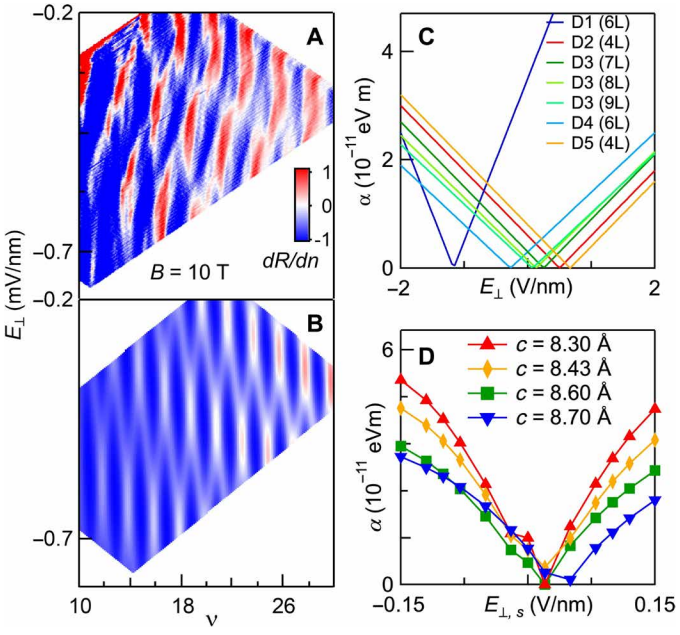

Fig. 4. Magnetotransport data and anomalously large SOC parameter. (**A** and **B**) $dR_{xx}/dn(n, E_\perp)$ and simulations at constant $B = 10$ T for device D1. (**C**) Extracted Rashba parameter and its dependence on $E_\perp$ for different devices. (**D**) DFT calculations of Rashba parameter versus $E_{\perp,s}$ for different c-axis lattice constants. Here, $E_{\perp,s}$ is the out-of-plane electric field used in calculations, which, due to screening, is substantially reduced from the experimental values calculated from external gate voltages.

c, which, according to DFT calculations, is an extremely effective "knob" to tune the SOC parameter. For instance, increasing c by a mere 1.9% (from 8.43 to 8.6 Å) results in a reduction of α_0 by 57% (from 0.89×10^{-11} to 0.57×10^{-11} eVm) (Fig. 4D). The small variations in interlayer spacing may arise from stacking faults: Although the γ phase is the most dominant phase in our crystals, TEM studies reveal high densities of stacking faults that are generated by dislocation dissociation or by growth, including ones with wrongly stacked monolayers (see figs. S1 and S2). The large electrostatic pressure generated by the displacement fields, which exceeds 20 MPa in our devices, may further compress the interlayer spacing. Another possibility is the nonlinear scaling of α with $E_\perp$ in the presence of stacking faults or twin boundaries. Although further work is required to ascertain the mechanism, these data show that Rashba SOC can be tuned through a much larger range than previously thought possible.

In summary, we observe the hallmarks of large Rashba SOC in few-layer InSe field effect transistor devices, where the unprecedented mobility enables quantitative extraction of the Rashba parameter. The two-dimensionality of the devices enables the SOC strength to be modulated by the layer thickness and by an electric field that breaks or compensates for the inversion symmetry. The possibility of piezo-SOC tuning, which has not been observed to date, warrants further theoretical and experimental investigation. The extraordinary tunability of SOC in 2D materials, as demonstrated here, can be exploited for a variety of phenomenon and devices, such as spin Hall effect, spin-orbit torque, and spin helix with long spin coherence time, with in situ control.

MATERIALS AND METHODS

Single crystals of InSe were synthesized from 6N-pure indium and 6N-pure selenium pellets in a ratio $In_{0.52}Se_{0.48}$. The starting materials were sealed in a quartz ampule and then vacuumed to 10^{-3} torr. They were subsequently prereacted by gradually heating the ampule to 800°C and kept at this temperature for 96 hours. After the reaction, the ampule was then placed into a radio frequency (RF) furnace where the RF power was gradually increased to raise the temperature up to 800°C. The ampule was then pulled through the hottest zone at a rate of 2 mm/hour.

Bulk InSe crystals are characterized by atomic-resolution high-angle annular dark-field scanning transmission electron microscopy using a probe aberration–corrected JEOL JEM-ARM200cF at

200 kV. TEM samples were made by focused ion beam in a Helios G4 DualBeam.

InSe and hBN crystals are exfoliated on polydimethylsiloxane into atomically thin sheets, with InSe thicknesses ranging from 4 to 10 layers. FLG for contacts is exfoliated on Si chips covered with 300-nm SiO_2. Using the dry-transfer technique (*29*) at room temperature, we assemble hexagonal hBN/few-layer InSe/hBN heterostructures, with contacts that consist of few FLG sheets. First, we pick up the FLG contacts, followed by InSe and, last, the bottom hBN. The exfoliation and stack assembly processes are performed in a glove box to minimize degradation. We then etch the heterostructure into the Hall bar geometry in two steps, first using SF_6 gas for hBN and then Ar gas for InSe (pressure, 15 mtorr; power, 60 W; average etch time, 15 s and 5 min for SF_6 and Ar, correspondingly), and deposit a layer of aluminum oxide covering the channel, followed by Cr/Au for electrodes and the top gate. The electrodes formed 1D contact to FLG.

Transport measurements are performed using SR830 and SR860 lock-in amplifiers at an ac bias current of 50 nA. All measurements are performed at base temperature in ^{3}He or pumped ^{4}He cryostats.

We used ab initio DFT to investigate the thickness dependence of functional properties in atomically thin InSe. DFT calculations were performed using the Vienna Ab initio Simulation Package (*30*, *31*) within the generalized gradient approximation with Perdew-Burke-Ernzerhof (*32*, *33*) functional. A plane-wave cutoff of 350 eV and Γ point–centered 12 × 12 × 1 k mesh for integration in reciprocal space are used (*34*). While we keep in-plane periodic boundary conditions, a vacuum of 12 Å is added perpendicular to the plane to minimize interactions between the periodic images of the films. Grimme's D2 (*35*) functional is used in all calculations to include the van der Waals interaction between the layers. When applying an external field on the slab, we turned on the dipole correction along the c axis to avoid interactions between the periodically repeated images. To determine the Rashba splitting for the bottom of the conduction band, fully relativistic SOC was included into the calculations in addition to the applied field. To accurately determine the position of the shifted conduction band minima, band energies were calculated for a large number of k points in the vicinity of the Γ point, and the Rashba parameter (α) is determined by $\alpha = \frac{\Delta E}{2\Delta k}$.

SUPPLEMENTARY MATERIALS

Supplementary material for this article is available at http://advances.sciencemag.org/cgi/content/full/7/5/eabe2892/DC1

REFERENCES AND NOTES

1. K. Momma, F. Izumi, *VESTA 3* for three-dimensional visualization of crystal, volumetric and morphology data. *J. Appl. Cryst.* **44**, 1272–1276 (2011).
2. Y. A. Bychkov, É. I. Rashba, Properties of a 2D electron gas with lifted spectral degeneracy. *JETP* **39**, 78 (1984).
3. Y. A. Bychkov, E. I. Rashba, Oscillatory effects and the magnetic susceptibility of carriers in inversion layers. *J. Phys. C Solid State Phys.* **17**, 6039–6045 (1984).
4. W. Witczak-Krempa, G. Chen, Y. B. Kim, L. Balents, Correlated quantum phenomena in the strong spin-orbit regime. *Ann. Rev. Condensed Matter Phys.* **5**, 57–82 (2014).
5. A. Manchon, H. C. Koo, J. Nitta, S. M. Frolov, R. A. Duine, New perspectives for Rashba spin–orbit coupling. *Nat. Mater.* **14**, 871–882 (2015).
6. R. Winkler, *Spin-orbit Coupling Effects in Two-Dimensional Electron and Hole Systems* (Springer-Verlag, 2003).
7. D. Marchenko, A. Varykhalov, M. R. Scholz, G. Bihlmayer, E. I. Rashba, A. Rybkin, A. M. Shikin, O. Rader, Giant Rashba splitting in graphene due to hybridization with gold. *Nat. Commun.* **3**, 1232 (2012).
8. Z. Wang, D.-K. Ki, J. Y. Khoo, D. Mauro, H. Berger, L. S. Levitov, A. F. Morpurgo, Origin and magnitude of 'Designer' spin-orbit interaction in graphene on semiconducting transition metal dichalcogenides. *Phys. Rev. X* **6**, 041020 (2016).
9. Z. Wang, D.-K. Ki, H. Chen, H. Berger, A. H. MacDonald, A. F. Morpurgo, Strong interface-induced spin–orbit interaction in graphene on WS_2. *Nat. Commun.* **6**, 8339 (2015).
10. L. A. Benítez, J. F. Sierra, W. S. Torres, A. Arrighi, F. Bonell, M. V. Costache, S. O. Valenzuela, Strongly anisotropic spin relaxation in graphene–transition metal dichalcogenide heterostructures at room temperature. *Nat. Phys.* **14**, 303–308 (2018).
11. A. Avsar, J. Y. Tan, T. Taychatanapat, J. Balakrishnan, G. K. W. Koon, Y. Yeo, J. Lahiri, A. Carvalho, A. S. Rodin, E. C. T. O'Farrell, G. Eda, A. H. C. Neto, B. Özyilmaz, Spin–orbit proximity effect in graphene. *Nat. Commun.* **5**, 4875 (2014).
12. B. Yang, M.-F. Tu, J. Kim, Y. Wu, H. Wang, J. Alicea, R. Wu, M. Bockrath, J. Shi, Tunable spin–orbit coupling and symmetry-protected edge states in graphene/WS_2. *2D Mater.* **3**, 031012 (2016).
13. T. Wakamura, F. Reale, P. Palczynski, S. Guéron, C. Mattevi, H. Bouchiat, Strong anisotropic spin-orbit interaction induced in graphene by monolayer WS_2. *Phys. Rev. Lett.* **120**, 106802 (2018).
14. S. Zihlmann, A. W. Cummings, J. H. Garcia, M. Kedves, K. Watanabe, T. Taniguchi, C. Schönenberger, P. Makk, Large spin relaxation anisotropy and valley-Zeeman spin-orbit coupling in WSe_2/graphene/h-BN heterostructures. *Phys. Rev. B* **97**, 075434 (2018).
15. M. M. Asmar, S. E. Ulloa, Symmetry-breaking effects on spin and electronic transport in graphene. *Phys. Rev. B* **91**, 165407 (2015).
16. M. Gmitra, J. Fabian, Graphene on transition-metal dichalcogenides: A platform for proximity spin-orbit physics and optospintronics. *Phys. Rev. B* **92**, 155403 (2015).
17. J. Y. Khoo, A. F. Morpurgo, L. Levitov, On-demand spin–orbit interaction from which-layer tunability in bilayer graphene. *Nano Lett.* **17**, 7003–7008 (2017).
18. T. S. Ghiasi, J. Ingla-Aynés, A. A. Kaverzin, B. J. van Wees, Large proximity-induced spin lifetime anisotropy in transition-metal dichalcogenide/graphene heterostructures. *Nano Lett.* **17**, 7528–7532 (2017).
19. D. Wang, S. Che, G. Cao, R. Lyu, K. Watanabe, T. Taniguchi, C. N. Lau, M. Bockrath, Quantum hall effect measurement of spin–orbit coupling strengths in ultraclean bilayer graphene/WSe_2 heterostructures. *Nano Lett.* **19**, 7028–7034 (2019).
20. J. Zeng, S.-J. Liang, A. Gao, Y. Wang, C. Pan, C. Wu, E. Liu, L. Zhang, T. Cao, X. Liu, Y. Fu, Y. Wang, K. Watanabe, T. Taniguchi, H. Lu, F. Miao, Gate-tunable weak antilocalization in a few-layer InSe. *Phys. Rev. B* **98**, 125414 (2018).
21. S. Takasuna, J. Shiogai, S. Matsuzaka, M. Kohda, Y. Oyama, J. Nitta, Weak antilocalization induced by Rashba spin-orbit interaction in layered III-VI compound semiconductor GaSe thin films. *Phys. Rev. B* **96**, 161303 (2017).
22. K. Premasiri, S. K. Radha, S. Sucharitakul, U. R. Kumar, R. Sankar, F.-C. Chou, Y.-T. Chen, X. P. A. Gao, Tuning rashba spin–orbit coupling in gated multilayer InSe. *Nano Lett.* **18**, 4403–4408 (2018).
23. E. Kress-Rogers, G. F. Hopper, R. J. Nicholas, W. Hayes, J. C. Portal, A. Chevy, The electric sub-band structure of electron accumulation layers in InSe from Shubnikov-de Haas oscillations and inter-sub-band resonance. *J. Phys. C Solid State Phys.* **16**, 4285–4295 (1983).
24. D. A. Bandurin, A. V. Tyurnina, G. L. Yu, A. Mishchenko, V. Zólyomi, S. V. Morozov, R. K. Kumar, R. V. Gorbachev, Z. R. Kudrynskyi, S. Pezzini, Z. D. Kovalyuk, U. Zeitler, K. S. Novoselov, A. Patanè, L. Eaves, I. V. Grigorieva, V. I. Fal'ko, A. K. Geim, Y. Cao, High electron mobility, quantum Hall effect and anomalous optical response in atomically thin InSe. *Nat. Nanotechnol.* **12**, 223–227 (2017).
25. J. C. J. M. Terhell, Polytypism in the III–VI layer compounds. *Prog. Cryst. Growth Charact.* **7**, 55–110 (1983).
26. J. Nitta, T. Akazaki, H. Takayanagi, T. Enoki, Gate control of spin-orbit interaction in an inverted $In_{0.53}Ga_{0.47}As/In_{0.52}Al_{0.48}As$ heterostructure. *Phys. Rev. Lett.* **78**, 1335–1338 (1997).
27. D. T. Do, S. D. Mahanti, C. W. Lai, Spin splitting in 2D monochalcogenide semiconductors. *Sci. Rep.* **5**, 17044 (2015).
28. S. J. Magorrian, in *Theory of Electronic and Optical Properties of Atomically Thin Films of Indium Selenide,* S. J. Magorrian, Ed. (Springer International Publishing, 2019), pp. 61–81.
29. L. Wang, I. Meric, P. Y. Huang, Q. Gao, Y. Gao, H. Tran, T. Taniguchi, K. Watanabe, L. M. Campos, D. A. Muller, J. Guo, P. Kim, J. Hone, K. L. Shepard, C. R. Dean, One-dimensional electrical contact to a two-dimensional material. *Science* **342**, 614–617 (2013).
30. G. Kresse, J. Hafner, *Ab initio* molecular dynamics for liquid metals. *Phys. Rev. B* **47**, 558–561 (1993).
31. G. Kresse, J. Hafner, *Ab initio* molecular-dynamics simulation of the liquid-metal–amorphous-semiconductor transition in germanium. *Phys. Rev. B* **49**, 14251–14269 (1994).
32. J. P. Perdew, K. Burke, M. Ernzerhof, Generalized gradient approximation made simple. *Phys. Rev. Lett.* **77**, 3865–3868 (1996).

33. P. E. Blöchl, Projector augmented-wave method. *Phys. Rev. B* **50**, 17953–17979 (1994).
34. H. J. Monkhorst, J. D. Pack, Special points for Brillouin-zone integrations. *Phys. Rev. B* **13**, 5188–5192 (1976).
35. S. Grimme, Semiempirical GGA-type density functional constructed with a long-range dispersion correction. *J. Comput. Chem.* **27**, 1787–1799 (2006).

Acknowledgment: We thank V. Fal'ko for stimulating discussion. **Funding:** The experiments are supported by NSF-DMR 1807928 and NSF-DMR 1807969. M.B. acknowledges the support of DOE BES DE-SC0020187. Y.W. and W.W. acknowledge primary funding by AFOSR project no. FA9550-18-1-0335. Computations were performed on the machines of the Ohio Supercomputer Center under project no. PAS0072. K.Wa. and T.T. acknowledge support from the Elemental Strategy Initiative conducted by the MEXT, Japan, through grant nos. JPMXP0112101001, JSPS KAKENHI and JP20H00354 and the CREST(JPMJCR15F3) JST. A portion of this work was performed at the National High Magnetic Field Laboratory, which is supported by National Science Foundation Cooperative Agreement No. DMR-1644779, and the State of Florida. **Author contributions:** D.Sh., P.S., and C.N.L. conceived the project. D.Sh. fabricated samples and performed measurements. P.S. assisted with sample fabrication. J.Y. and D.Sm. assisted with measurements. D.Sh., M.B., and C.N.L. analyzed and interpreted the data. S.M., W.Z., R.B., and L.B. synthesized InSe crystals. Y.W. and W.W. performed DFT calculations. Y.X., K.We., R.B., and T.S. performed crystallographic measurements and analysis. K.Wa. and T.T. provided hBN crystals. D.Sh. and C.N.L. wrote the manuscript. All authors discussed and commented on the manuscript. **Competing interests:** The authors declare that they have no competing interests. **Data and materials availability:** All data needed to evaluate the conclusions in the paper are present in the paper and/or the Supplementary Materials. Additional data related to this paper may be requested from the authors.

Submitted 17 August 2020
Accepted 7 December 2020
Published 29 January 2021
10.1126/sciadv.abe2892

Citation: D. Shcherbakov, P. Stepanov, S. Memaran, Y. Wang, Y. Xin, J. Yang, K. Wei, R. Baumbach, W. Zheng, K. Watanabe, T. Taniguchi, M. Bockrath, D. Smirnov, T. Siegrist, W. Windl, L. Balicas, C. N. Lau, Layer- and gate-tunable spin-orbit coupling in a high-mobility few-layer semiconductor. *Sci. Adv.* **7**, eabe2892 (2021).

Layer- and gate-tunable spin-orbit coupling in a high-mobility few-layer semiconductor

Dmitry Shcherbakov, Petr Stepanov, Shahriar Memaran, Yaxian Wang, Yan Xin, Jiawei Yang, Kaya Wei, Ryan Baumbach, Wenkai Zheng, Kenji Watanabe, Takashi Taniguchi, Marc Bockrath, Dmitry Smirnov, Theo Siegrist, Wolfgang Windl, Luis Balicas and Chun Ning Lau

Sci Adv **7** (5), eabe2892.
DOI: 10.1126/sciadv.abe2892